metals

MDPI

Review

Elaboration of Metallic Materials by SPS: Processing, Microstructures, Properties, and Shaping

Jean-Philippe Monchoux [1,2,*], Alain Couret [1,2], Lise Durand [1,2], Thomas Voisin [3], Zofia Trzaska [4,5] and Marc Thomas [6]

1 Centre d'Elaboration de Matériaux et d'Etudes Structurales, Centre National de la Recherche Scientifique, Unité Propre de Recherche 8011, 29 rue J. Marvig, BP 94347, CEDEX 4, 31055 Toulouse, France; alain.couret@cemes.fr (A.C.); lise.durand@cemes.fr (L.D.)
2 Université Toulouse III—Paul Sabatier, 118 Route de Narbonne, CEDEX 9, 31062 Toulouse, France
3 Lawrence Livermore National Laboratory, 7000 East Av., Livermore, CA 94550, USA; voisin2@llnl.gov
4 Institut de Chimie et des Matériaux Paris-Est, Unité Mixte de Recherche 7182, 2-8, rue Henri Dunant, 94320 Thiais, France; zofia.trzaska@univ-paris13.fr
5 Université Sorbonne Paris Nord, 99, Avenue Jean-Baptiste Clément, 93430 Villetaneuse, France
6 ONERA—The French Aerospace Lab, Department of Materials and Structures, Université Paris-Saclay, 29 Avenue de la Division Leclerc, BP 72, 92322 Châtillon CEDEX, France; marc.thomas@onera.fr
* Correspondence: monchoux@cemes.fr

Abstract: After a few decades of increasing interest, spark plasma sintering (SPS) has now become a mature powder metallurgy technique, which allows assessing its performances toward fabricating enhanced materials. Here, the case of metals and alloys will be presented. The main advantage of SPS lies in its rapid heating capability enabled by the application of high intensity electric currents to a metallic powder. This presents numerous advantages balanced by some limitations that will be addressed in this review. The first section will be devoted to sintering issues, with an emphasis on the effect of the electric current on the densification mechanisms. Then, typical as-SPS microstructures and properties will be presented. In some cases, they will be compared with that of materials processed by conventional techniques. As such, examples of nanostructured materials, intermetallics, metallic glasses, and high entropy alloys, will be presented. Finally, the implementation of SPS as a technique to manufacture complex, near-net shape industrial parts will be discussed.

Keywords: SPS; metals; TiAl; microstructure; mechanical properties; shaping

check for updates

Citation: Monchoux, J.-P.; Couret, A.; Durand, L.; Voisin, T.; Trzaska, Z.; Thomas, M. Elaboration of Metallic Materials by SPS: Processing, Microstructures, Properties, and Shaping. *Metals* **2021**, *11*, 322. https://doi.org/10.3390/met11020322

Academic Editor: Eric Hug

Received: 18 January 2021
Accepted: 7 February 2021
Published: 12 February 2021

Publisher's Note: MDPI stays neutral with regard to jurisdictional claims in published maps and institutional affiliations.

Copyright: © 2021 by the authors. Licensee MDPI, Basel, Switzerland. This article is an open access article distributed under the terms and conditions of the Creative Commons Attribution (CC BY) license (https://creativecommons.org/licenses/by/4.0/).

1. Introduction

Spark plasma sintering (SPS) has become a widely used processing technique for a broad class of materials, including ceramics, metals, and polymers. Consequently, significant improvements were achieved since the review conducted by Orru et al. [1] in 2009, allowing SPS to reach pre-industrialization. Early on, the ability of SPS to rapidly process many different materials with improved microstructures and properties was attributed to electricity-induced phenomena, such as the occurrence of sparks or plasma at the powder particle interfaces (which the process was named after), the involvement of electromigration, electroplasticiy, and so on. However, after two decades of investigations, it is now possible to discuss more accurately these early hypotheses, and to establish more firmly its physical principles.

In this chapter, we will concentrate on the case of the metallic materials. Regarding potential electrical effects, these materials exhibit the particularity of a high electric conductivity. Therefore, they have been particularly the subject of investigation of electrically-induced effects. We will present studies devoted to these questions, but also, more generally, to the densification mechanisms and kinetics. Then, we will present the original microstructures, which can be achieved, characterized often by nanostructuration, and we will present results showing the relation between the microstructures obtained by

SPS and those predicted by the equilibrium phase diagram. This will lead us to make a review of materials, which have been the subject of particular interest regarding their processing by SPS: intermetallics, nanostructured materials, metallic glasses, and high entropy alloys. Then, because processing of parts in complex geometries is becoming a major issue, we will deal with the necessary steps involved to achieve this goal: thermo-mechanical modeling, upscaling, and shaping.

2. Overview of the SPS Process

SPS technology consists in densifying powders by applying high electric current pulses under mechanical pressure. This results in rapid heating and compaction of the powder into fully dense materials. As shown in the reviews of Orru et al. [1] and of Munir et al. [2], the principle of the SPS originates in 1922. The ideas of local heating at the particle contacts was proposed in 1945, and the hypothesis of vaporization of superficial oxide layers by dielectric breakdown was formulated in the 1950s. The term *spark sintering* appeared in 1965, and Inoue enriched these concepts by describing phenomena, such as electric discharge, ionization, or local melting, and developed devices based on the use of high frequency electric currents. The works of Inoue lead to the development of Be-based materials for missiles at the Lockheed Corporation at the end of the 1960s. However, the extensive spreading of the current-assisted sintering technologies occurred at the beginning of the 1990s, when the Sumitomo Coal Mining company developed the so-called *spark plasma sintering* technology, based on patents of the 1960s. Since then, the number of works devoted to the SPS approach has increased very rapidly. For example, an analysis of the number of articles published per year containing the keywords "spark plasma sintering" is given in Figure 1. It shows an impressive increase in publications since the first time this term was encountered in literature, in 1994. Among this production, an analysis of the review of Orru et al. in 2009 [1] shows that the studies on metallic systems represent ≈ 15% of the total, a proportion probably stable over time.

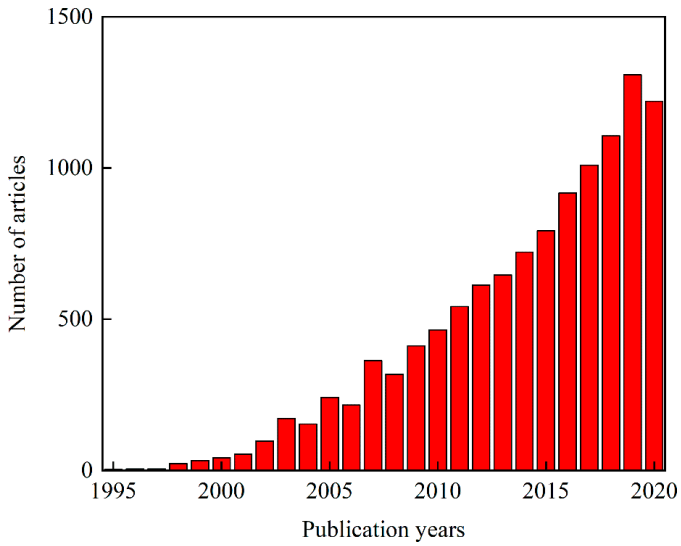

Figure 1. Number of articles per year related to spark plasma sintering (SPS) technology (source: Web of Science).

A simplified schematic of the powder sintering setup as found in most commercial SPS machines is depicted in Figure 2. The powder is filled inside a graphite mold, generally made of graphite, consisting in a cylindrical container closed by two compression electrodes, and this assembly is introduced into an evacuated chamber. As a high pressure (typically around 100 MPa) and a high intensity current are applied through the pistons, the entire setup, including the powder if conductive, rapidly heats up by Joule effect. In fact, because the heat production occurs internally, high heating rates can be achieved

(typically 50–1000 °C/min, depending on the setup, material, and intensities). As a result, short processing times (5–60 min) can be achieved. Figure 3 gives an example of a typical processing cycle for TiAl disks 36 mm in diameter and 8 mm thick. It can be seen, in this example, that the current intensity reached 3000 A. Because the temperature is usually not measured at the sample but either on the external surface of the die or inside one of the electrodes, a few cm away from the sample, a temperature gradient between the measure and the sample exists. In this case, corrections can be applied based on experimental calibrations or simulations. This will be discussed in Section 5.

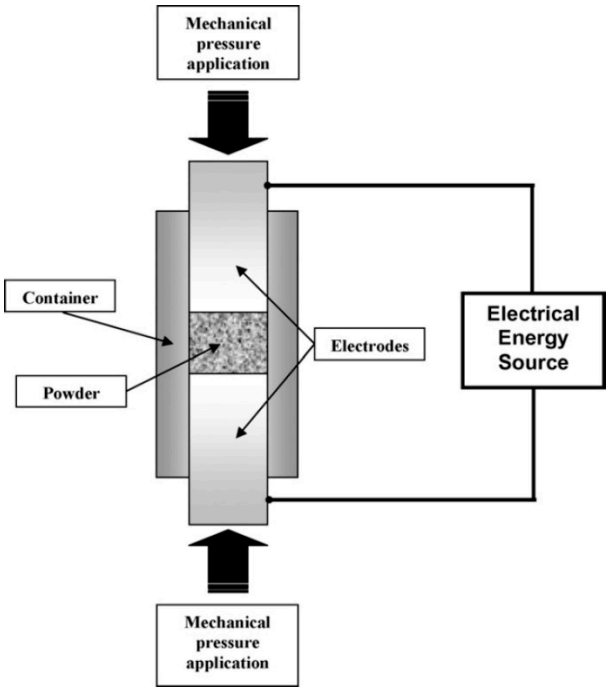

Figure 2. Schematic representation of the SPS process [1]. Reproduced with permission from *Materials Science and Engineering: R*, published by Elsevier, 2009.

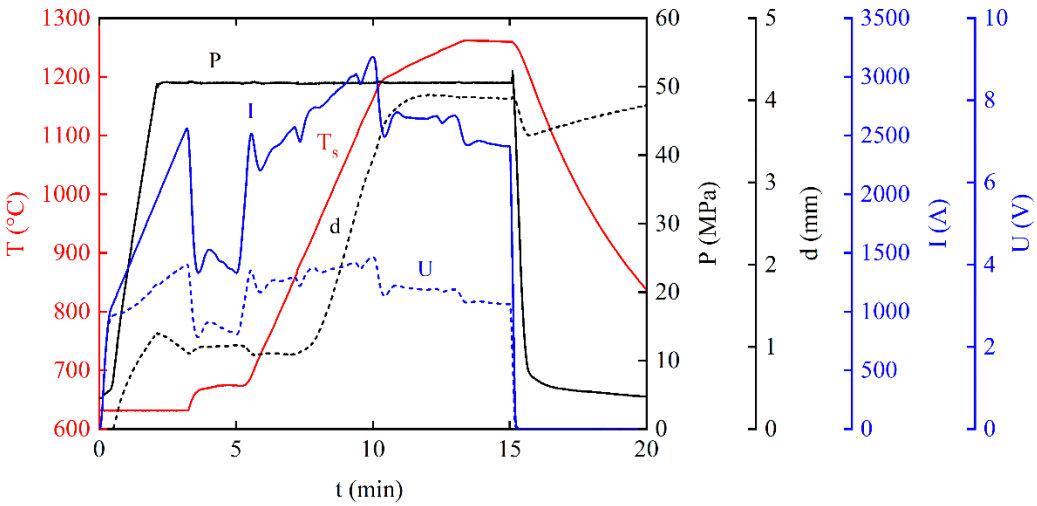

Figure 3. Evolution of the SPS parameters during the processing of a metallic TiAl alloy, in the case of a 36 mm sample (T_s: corrected sample temperature, P: applied mechanical pressure, I: intensity, U: voltage and d: sample thickness reduction).

3. Densification Mechanisms and Kinetics

It has been suggested that the high intensity electric current applied upon processing could intrinsically influence the sintering kinetics and the densification mechanisms [1–3]. We present here the main efforts dedicated to verifying this hypothesis.

3.1. Microscopic Densification Mechanisms

Several mechanisms that can be induced by the high-intensity electrical current during SPS can be classified as follow: (i) dielectric breakdown of the oxide layers at the surface of the powder particles. (ii) Arcs and plasma generation between powder particles. (iii) Local overheating due to a current density increase at the contact between powder particles. (iv) Activation of electromigration and electroplasticity.

Mechanisms (i) and (ii) have been first proposed by Tokita [3]. Breakdowns of superficial oxide layers, mechanism (i), were reported in many studies [4–7], but without providing convincing experimental evidences. Arcing, as in mechanism (ii), has been on the contrary more clearly observed between adjacent Cu powder particles 550 μm in diameter (Figure 4) [8]. However, in this work the applied pressure was very low, which did not reproduce the conditions encountered during an actual SPS cycle. Detection of arcs by emission spectroscopy has been attempted by two teams. Plasma was reported in a W powder for applied voltages >50 V by Saunders et al. [9]. Conversely, Hulbert et al. [10] concluded to the absence of plasma in various metallic powders (Al, Mg, Zn) for voltages ≈ 1–2 V, which are closer to that observed in typical SPS experiments. Even though spark and/or plasma events may still happen at the onset of sintering, the heavy plastic deformation of the interparticle contact regions due to the applied high pressure may too quickly remove the geometrical singularities at the origin of electric current intensification and arcing.

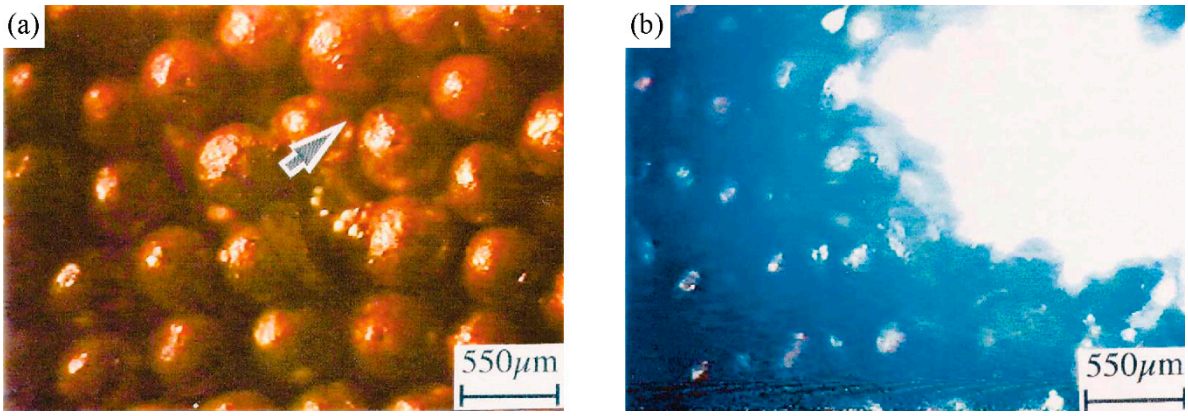

Figure 4. (**a**) Cu powder particles 550 μm in diameter. (**b**) Generation of an electric arc by a current pulse of 6700 A/cm^2 during 100 ms, at the location indicated by an arrow in Figure (**a**) [8]. Reproduced with permission from *Materials Science and Engineering: A*, published by Elsevier, 2003.

Local Joule overheating at the contacts between powder particles, mechanism (iii) has mainly been investigated theoretically. In the early works, very elevated local current densities, leading to local high overheating at the contacts (up to 10,000 °C), were computationally calculated [8,11]. The main limitation of these simulations is that they did not consider heat conduction within the particles, which was later shown to play a major role [12–16]. Even though more recent simulations predict local current densities as high as ≈ 5 × 10^4 A/cm^2 at the contacts between particles [15–17], it has been shown that, for regular-size powder particles (≈ 100 μm), the temperature homogenization by heat conduction takes only milliseconds, which was not compatible with stabilization of "hot spots" at the particle contacts [15,16]. Few experimental works with FeAl [18] and metallic glasses [19] concluded local overheating, but clear and direct evidence could not be

provided. Therefore, the formation of "hot spots" at the regions of contact between powder particles due to local electrical current concentrations is still debated in the literature.

Finally, the activation of metallurgical effects by electric currents, mechanisms (iv), has been considered, because the high current densities in the particles contact regions ($\approx 5 \times 10^4$ A/cm^2) are near or above the activation threshold for electroplasticity (10^3–10^6 A/cm^2) [20–22] and electromigration (10^2–10^3 A/cm^2) [2]. For example, model experiments with 3 mm Cu spheres in contact with Cu plates showed enhanced growth rates of the sphere-plate contact zones with currents $\approx 5 \times 10^2$ A/cm^2 [17]. This effect, which could account for increase in densification rate of metallic powders by the current, was interpreted by electromigration phenomena. However, another interpretation can also be proposed. When the size of the powder particle increases, and reaches millimeters and above, the thermal equilibration of the powder particles takes longer time [12,13], and hot spots can therefore be stabilized in the contact regions. Consequently, the local increase of the temperature can lead to acceleration of plastic deformation by creep. Other experimental investigations have been performed by focused ion beam and transmission electron microscopy (TEM) in the contact regions between powder particles in TiAl [23] and Ni [24]. It has been shown that the elementary deformation mechanisms were dislocation glide and climb, followed by dislocations recovery and recrystallization. For example, Figure 5 shows TEM images of a thin foil extracted in the contact region between two Ni powder particles [24]. High dislocation densities, and recovery walls, can be observed. This suggests that the observed mechanisms, which are those classically involved in power-law creep, are not significantly modified by the electric current.

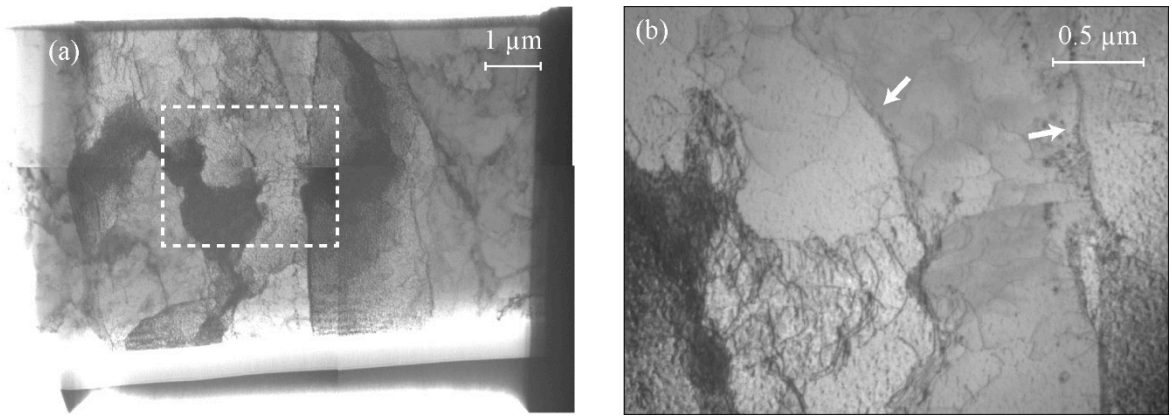

Figure 5. (**a**) TEM thin foil extracted from the contact region between two particles during densification of a Ni powder by SPS. (**b**) Zoom-in corresponding to the white dashed rectangle in (**a**) showing the presence of dislocations wall associated to dislocation recovery mechanisms [24]. Reproduced with permission from *Metallurgical and Materials Transactions: A*, published by Springer Nature, 2018.

3.2. Influence of High Intensity Currents on Powder Densification Kinetics

The effect of high intensity currents on the metallic powder densification at macroscopic scale has been the subject of several studies that gave contradictory results. For example, Figure 6 shows that when increased currents are applied to a Ni powder, by use of devices forcing all of the current to flow through the sample (setup 2), the final density of the sample is about 5% higher than that obtained in current-insulated experiments (setup 3), keeping the other parameters (temperature, pressure, dwell time, etc.) identical [25]. Similarly, Aleksandrova et al. [26] observed a density increase of Cu specimens when applying currents of 1000 A/cm^2, compared with experiments without current. On the contrary, a comparison between SPS and hot pressing with Cu [27] and TiAl [28] powders highlighted similar densification kinetics (density as a function of time) independently of the process employed.

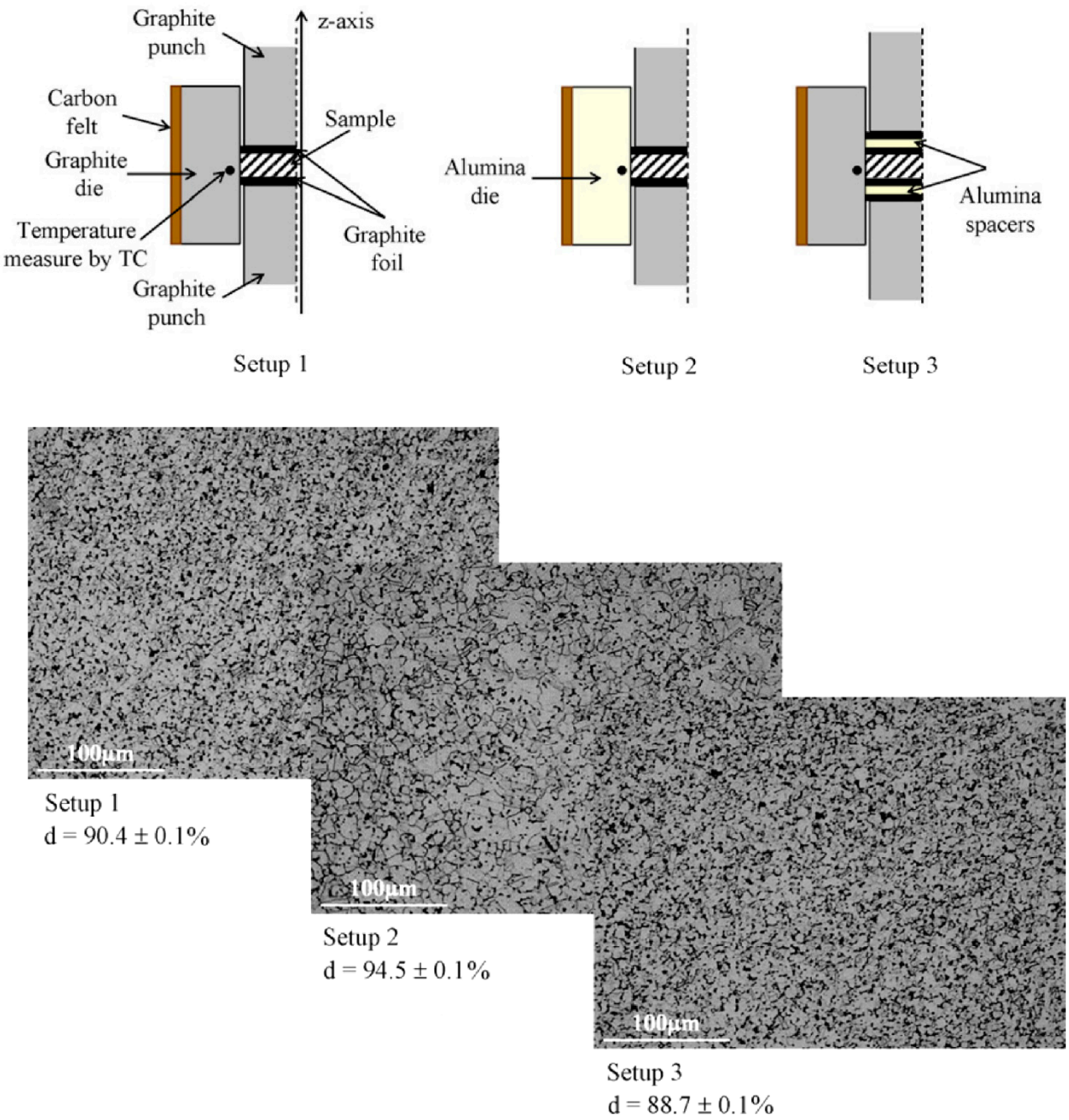

Figure 6. Relative density *d* of a Ni powder submitted to normal SPS conditions (setup 1), and to conditions where all of the SPS current flows through the sample (setup 2) and where the sample is electrically insulated (setup 3). Note in particular the difference in relative density *d* between samples processed using setup 2 (*d* = 94.5%) and setup 3 (*d* = 88.7%), showing an increase of sample relative density of about 5% due to the electric current [25]. Reproduced with permission from *Journal of Alloys and Compounds*, published by Elsevier, 2010.

3.3. Conclusions

What the investigations reported in this section agree on is that it is not possible to definitively conclude on the role of high intensity electric currents on the densification mechanisms and kinetics besides providing an effective heat source. Macroscopic effects are at most moderate [26], limited [25] or inexistent [27,28]. Moreover, at the microscopic scale, with the noticeable exception of the study of Yanagisawa et al. [8], no evident phenomena have been experimentally detected. The densification mechanisms are consequently similar to those classically involved in densification theories: deformation of the powder particles

by power-law creep involving dislocations glide and climb, followed by recovery and recrystallization [23,24]. Therefore, it can reasonably be stated that the densification of metallic powders by SPS experiments is not governed by electrical effects. As such, the process can be adequately modeled using Norton law constitutive relations, as will be detailed in Section 5.

4. As-SPS Microstructure and Mechanical Properties

As a powder metallurgy technique, the SPS primarily purpose is to densify powders to obtain bulk metallic materials of controlled density. However, because the sintering takes place at high temperatures, it is also possible to optimize the microstructures. In many cases, this results in improved mechanical properties. Moreover, the rapid densification capability of the SPS technique allows obtain nanostructured or metastable materials by using very short thermal cycles. Another important advantage of the SPS technique is the microstructure homogeneity, which is generally more satisfactory than with other techniques, such as casting for example. However, the distribution of the electric current during SPS is often heterogeneous throughout the samples, which causes temperature gradients, especially for large samples, resulting in possible microstructure variations. Therefore, a significant effort has been dedicated to model the temperature fields in samples and molds toward optimizing the temperature distribution in large specimens, as will be discussed in Section 5. These microstructures heterogeneities are nevertheless less pronounced than with casting, because in this latter case solidification leads to many structural defects: cracks, porosities, contaminations, segregations and so on. Moreover, the problem of temperature heterogeneity in large parts tends to be mastered, by adapting the geometry of the molds, or by developing the so-called "hybrid" SPS technology, which provides additional heat sources leading to decrease of the temperature gradients within the parts. Therefore, the SPS shows now a high potential for developing advanced materials, for parts of increasing dimensions. This section is thus dedicated to discuss selected studies that best illustrate the potential of SPS to tune microstructures and improve the resulting mechanical properties.

4.1. Equilibrium Microstructures

Because of the rapidity of the SPS technique, it is anticipated that the phases and microstructures of metallic alloys can differ from those at equilibrium as predicted by the phase diagrams. This point has been investigated in the case of TiAl alloys, for which processing by conventional techniques in suitable fields of the binary phase diagram lead to well referenced near γ, duplex, and lamellar microstructures [29]. It has been shown that, in the case of the simplest TiAl-based GE alloy (Ti-Al_{48}-Cr_2-Nb_2), manufacturing by SPS leads to an accurate correspondence with the binary phase diagram (Figure 7 [30]). Each microstructure exhibits a specific mechanical response to uniaxial tension at room temperature and uniaxial tensile creep testing at high temperature. This provides the opportunity to find a microstructure with an optimized balance between room temperature ductility and high temperature properties. Unfortunately, such a compromise cannot be reached with the Ti-Al_{48}-Cr_2-Nb_2 composition as show in Figure 7. The duplex microstructure offering the best ductility exhibits high creep deformation rate and limited lifetime (Figure 7d,f). However, because the obtained microstructures were those predicted by the phase diagrams, it was possible to design materials of more complicated chemistries and microstructures, based on theoretically predicted phase diagrams, to improve the mechanical properties [30,31]. Thus, the beneficial roles of W on the creep resistance, through reduction of the diffusion rates, and that of B on the limitation of grain growth, through grain boundary pinning on TiB_2 precipitates, have been investigated. This resulted in the so-called IRIS alloy, of Ti-48Al-2W-0.1B composition, which strength at high temperature was higher than alloys elaborated by other techniques (Figure 8 [32,33]).

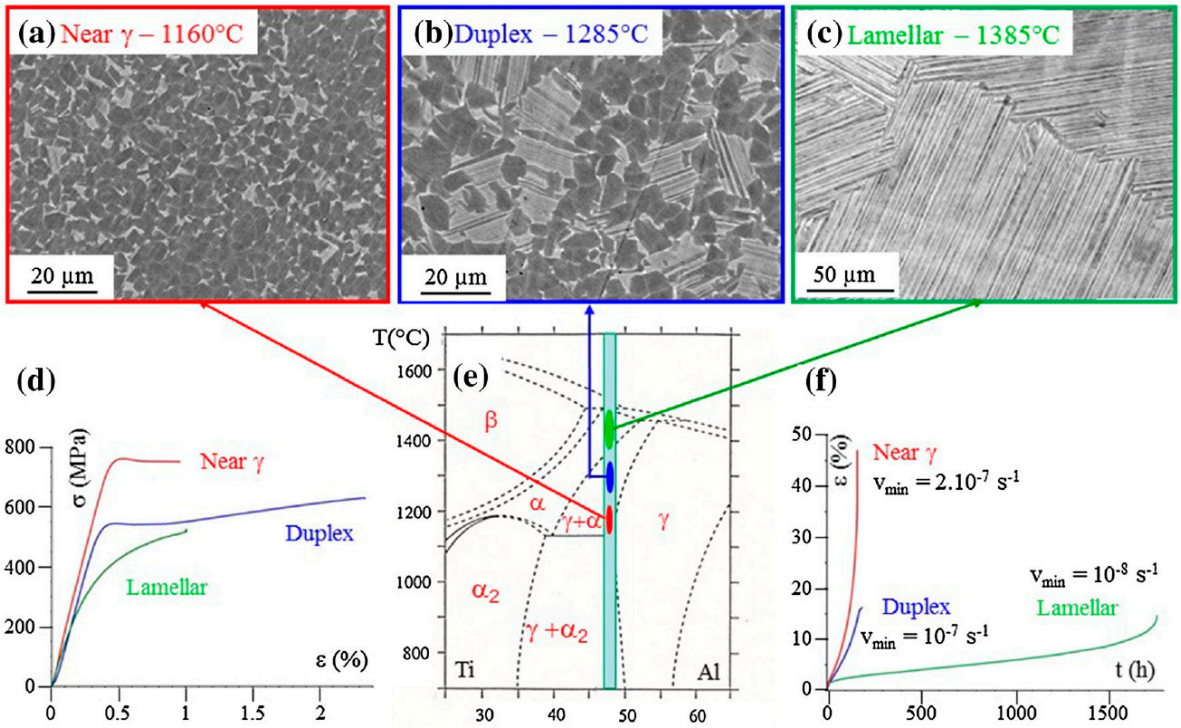

Figure 7. (**a**–**c**) Near γ, duplex, and lamellar microstructure of the Ti-Al_{48}-Cr_2-Nb_2 alloy obtained by elaboration by SPS, compared with the binary phase diagram of this alloy (**e**). Mechanical properties in tension at room temperature (**d**) and in creep (700 °C—300 MPa) (**f**) of the corresponding materials [30]. Reproduced with permission from *Journal of the Minerals, Metals and Materials Society*, published by Springer Nature, 2017.

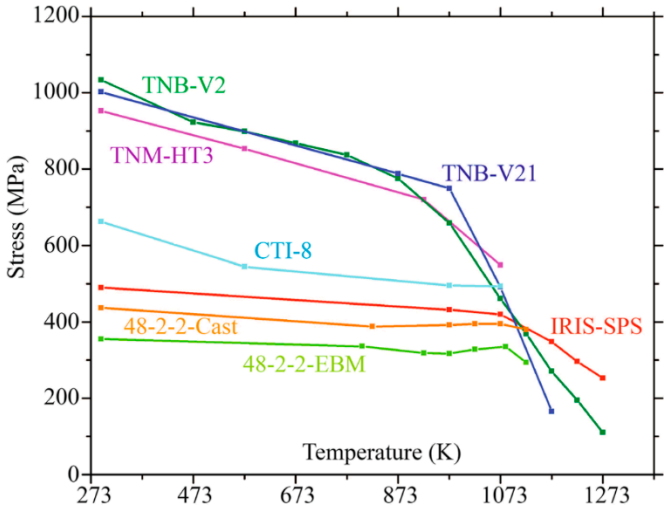

Figure 8. Variation of the yield stress as a function of temperature of the TiAl IRIS alloy elaborated by SPS, compared with that of alloys elaborated by other techniques (TNM-HT3: forging, TNB-V2, TNB-V21 and CTI-8: extrusion, 48-2-2: casting, 48-2-2-EBM: electron beam melting) [33]. Reproduced with permission from *Metallurgical and Materials Transactions: A*, published by Springer Nature, 2016.

4.2. Nanostructured Materials

Limiting the grain coarsening during manufacturing is one of the main advantages of SPS. Densification can occur fast enough for samples to be held at high temperature over short period of time, typically in the order of minutes. Therefore, nanostructured materials can be obtained with potentially original mechanical properties.

Various nanostructured metals and alloys were obtained by SPS using nanopowders such as Cu [34], TiNi [35], Al [7,36], and W [37]. For example, in the case of Al, the use of

appropriate SPS parameters allows to keep an extremely fine microstructure, the average grain size being in the order of 50 nm [7]. In addition, using nanopowders [38–42], or micrometric mechanically activated powders [43–45], nanostructured Ni materials have successfully been obtained. In particular, these routes allowed elaboration of nanomaterials exhibiting very high-accumulated strains during cyclic tests [38], as well as significantly enhanced strength (Figure 9) [43]. However, in the case of nanopowders, oxides at the surface of the powder particles were found to affect the cohesion of the material [42], leading to low ductility in compression [39] and tension [41]. Incidentally, these results indicate that a removal of the superficial oxide layers by electric arcs and/or plasma, as proposed in several studies [4–7], does not seem to operate. Finally, original harmonic microstructures consisting in nanograins surrounding large grains could be stabilized with β-Ti due to the rapidity of the SPS process (Figure 10) [46–49]. These materials exhibited enhanced resistance under monotonic solicitation [46,47] and fatigue [48,49].

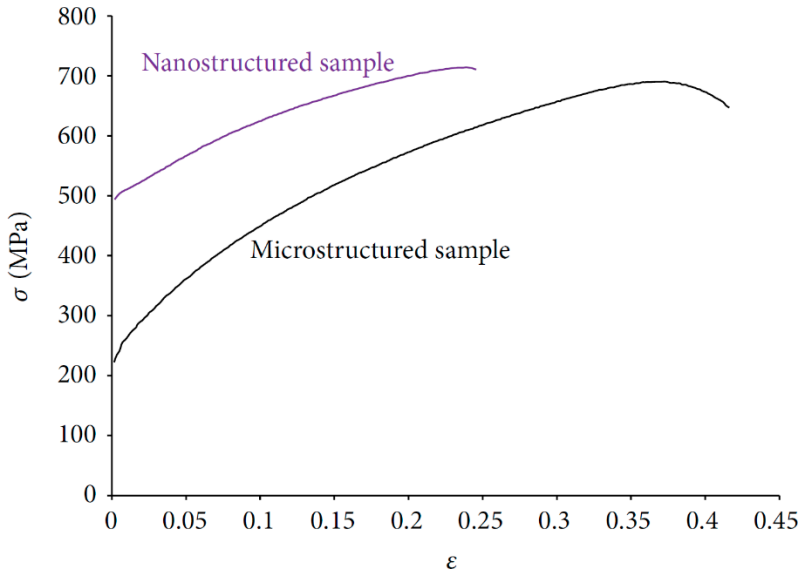

Figure 9. Tensile curves of micro- and nanostructured Ni materials elaborated by SPS [43]. Reproduced with permission from *Journal of Nanomaterials*, published by Hindawi, 2013.

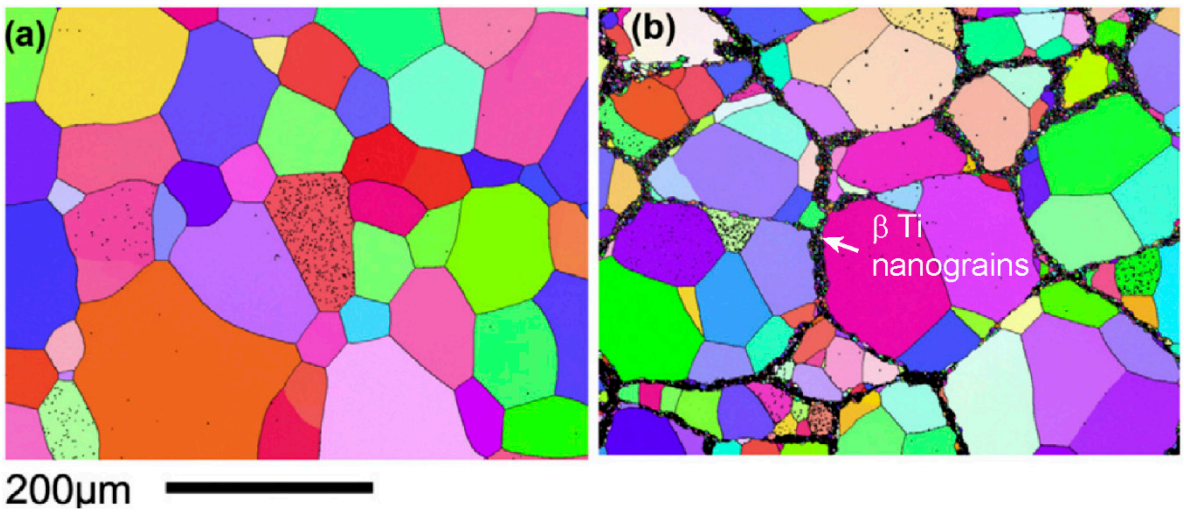

Figure 10. SEM electron back-scattered diffraction inverse pole figure maps of the β-Ti phase comparing the coarse grain microstructure of a material conventionally processed (**a**), to the harmonic microstructure, consisting of large grains surrounded by nanograins, of a material processed by SPS (**b**) [48]. Reproduced with permission from *Scripta Materialia*, published by Elsevier, 2017.

4.3. Metallic Glasses

The SPS technique has shown a high potential for developing amorphous metallic materials. This is first the consequence that the pre-alloyed powders can be prepared by atomization, the very fast cooling rates of the liquid alloy droplets (10^5–10^8 °C/s) [50] during the atomization process, favoring solidification in amorphous state. Therefore, the atomization route has been successfully employed since the late 1970s [51]. Then, to avoid devitrification during processing of the amorphous powder at high temperature, the SPS method is particularly interesting in reason of its rapidity. As such, many metallic glasses have been developed as recently reviewed by Perrière et al. [52]. However, in some cases with Zr-based metallic glasses, devitrification was observed at the powder particle contacts at the early stages of densification, a phenomenon that was interpreted by local overheating effects [19,53]. Such devitrification effects can be detrimental for the development of metallic glasses by SPS, and need now to be better controlled.

4.4. High Entropy Alloys

The use of the SPS for developing high entropy alloys (HEA) results from the better homogeneity obtained by this technique as compared to casting, and also from the very fine microstructures, which can be achieved. However, sintering of elemental powders is most of the time not possible, because of incomplete reaction at the end of the elaboration. Therefore, mechanical alloying (MA) is frequently employed before elaboration by SPS. Surprisingly, there were only few attempts so far to investigate the gas atomization technique [54,55] despite the wide use of this technique to produce pre-alloyed powders. Therefore, the works reported below only refer to materials obtained by SPS after MA.

For example, the MA + SPS route allowed to obtain $Co_{25}Ni_{25}Fe_{25}Al_{7.5}Cu_{17.5}$ alloys exhibiting strength more than eight times higher than materials elaborated by arc melting [56], $Ni_{1,5}Co_{1,5}CrFeTi_{0,5}$ alloys exhibiting very good combination of strength and ductility [57], and other high-strength alloys (e.g., AlCoCrCuFe and NiCoCrCuFe [58], $Al_{0.75}FeNiCrCo$ [59], $Ni_{1.5}CoCuFeCr_{0.5}$ [60]). In all of these cases, the interest of the SPS was the preservation of the nanostructuration. In addition, the possibility to mix different powders by SPS allowed obtaining self-lubricating CoCrFeNi-(Ag, BaF2/CaF2) composites that can reach friction coefficients below 0.26 [61].

In these studies, the rapid densification by SPS allowed retaining nanostructures, which partially explains the high strength. Note that the potential powder contamination during MA by the milling medium or the environment can be overcome by developing suitable methodologies [62]. The main disadvantage of MA remains the long process time. For that, powder gas atomization appears more suited as it has demonstrated successful obtention of several pre-alloyed powders with metals of very different melting points, such as Al, Ti, Re, and W [63].

4.5. Conclusions

The examples shown in this part demonstrate that the SPS allows elaborating materials with elevated mechanical properties. Moreover, the microstructures can be accurately predicted provided that the theoretical phase diagram is known. Therefore, it has been attempted, in some cases, to manufacture parts of larger sizes and of increased geometrical complexity. This is the subject of the next section.

5. Towards Elaboration of Complex Parts

Beside manufacturing materials, it has been demonstrated that the SPS technique was also efficient for shaping. However, it has to be underlined that, if some achievements look impressive, the development of shaping by SPS is not straightforward. Because the processing occurs by submitting a powder to a uniaxial pressure at high temperature, many constraints have to be considered: the electrodes move in only one direction, the volume occupied by the parts evolves due to densification of the powder, the temperature is not homogeneous within the material, and so on. Therefore, it has been proved useful to first

develop predictive modeling strategies, based on multi-physics finite element methods coupling the various physical parameters of the technique (electric fields, temperature gradients, stress distribution). After these modeling studies, it is generally necessary to develop suitable SPS cycles for parts of large dimensions. Due to energy limitations, most laboratory SPS equipment have a limit in maximum sample size that is, even though material dependent, usually around 5 cm in diameter for a couple cm in thickness. Finally, shaping of small or large specimen is attempted, using specially designed molds. This is this last part, which is by far the most critical, and different approaches have been proposed.

5.1. Modeling of the SPS Process

Modeling the SPS process is a complex task that requires accounting for several physics at once. The case of conducting metallic materials has been considered in the following references: [64–79]. As depicted by Achenani et al. [78], the ongoing modeling effort can be divided in two categories: thermoelectric coupling to simulate temperature gradients in fully-dense, static conditions [64–67,70,74,76,78,79], and stress distribution calculations to model the densification kinetics [28,68,69,71–73,75,77].

5.1.1. Thermoelectric Coupling

Knowing the temperature distribution in SPS samples during processing is key to control the temperature gradients and ensure full densification and homogeneous microstructures. However, the temperature fields within the samples and molds are complex, because they result from two main contributions. The first one is the heat generated by the Joule effect under the influence of the high intensity electric current. The current distribution being non-uniform, the heat production exhibits also high variations within the sample/mold assembly. The second is the cooling, by heat radiation from the external surfaces and by heat transfer towards the water-cooled electrodes (note that exothermic or endothermic reactions within the samples are here not considered.) Because the influence of these contributions on the resulting temperature fields can be difficult to anticipate, modeling has proved very useful. Thus, the finite element method (FEM) has been widely employed to predict the temperature fields within the sample/molds assembly. Equations coupling the contributions of heat production by Joule effect and of heat conduction are solved, which are generally of the following forms:

$$\nabla \times \nabla(V) = 0, \tag{1}$$

$$\nabla \times (-k\nabla T) + \rho c_p \left(\frac{\partial T}{\partial t}\right) = Q, \tag{2}$$

$$Q = \sigma(\nabla V)^2, \tag{3}$$

where V: electric potential, k: thermal conductivity, ρ: density, c_p: thermal capacity, σ: electrical conductivity, T: temperature and t: time. Using this approach, Anselmi-Tamburini et al. [80] showed that the current density profile across the sample and mold is significantly non-uniform and highly depending on the electrical conductivity of the sample (Figure 11a,b). Consequently, the temperature field is also non-uniform within the molds and the samples (Figure 11c). However, the shape of the thermal gradient cannot be deduced in a straightforward manner from the current density profile, and modeling proves here quite useful. By comparing insulating and conducting materials, Vanmeensel et al. [67] concluded that the amplitude of the temperature gradient was more elevated in the latter case (Figure 12). Similar simulations were developed and experimentally validated for TiAl alloys by Voisin et al. [74]. As discussed in Section 4.1, Ti-Al_{48}-Cr_2-Nb_2 undergoes a microstructure transition from duplex to lamellar at 1335 °C. This was used as an indicator of the local temperature to validate FEM models predictions. It was thus shown that the predicted temperature gradients in TiAl samples was depending on the geometry of the setup, in quantitative agreement with experimental metallographic observations (Figure 13). In particular, the use of elongated molds allowed to move away from each

other the hot spots created at the extremities of the molds, and consequently to lower the temperature gradients in the parts.

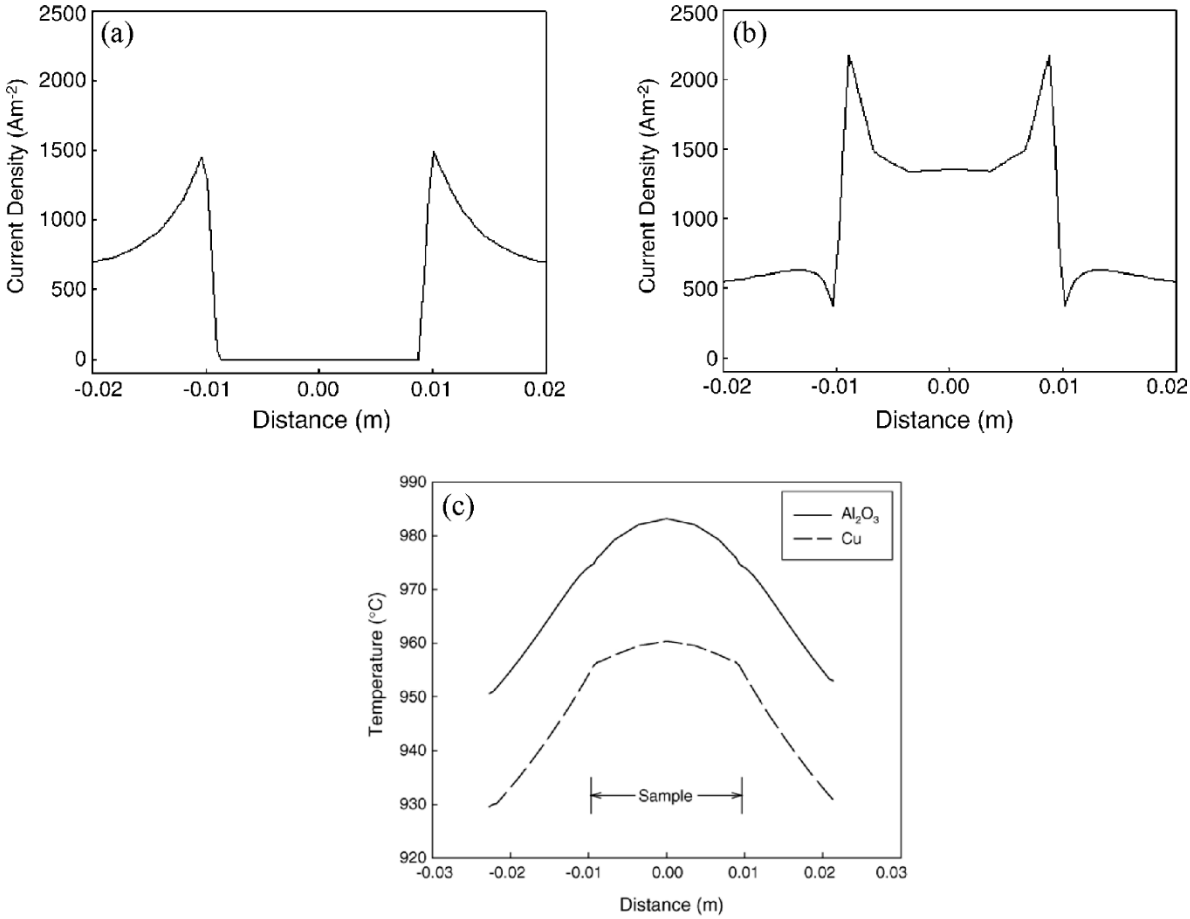

Figure 11. Radial current density distribution for non-conducting and conducting materials (applied voltage: 5V): Al_2O_3 (**a**) and Cu (**b**). Temperature distribution for Al_2O_3 and Cu (constant current applied: 1000 A) (**c**). In all cases, the profile is passing through the center of the samples and though the graphite molds surrounding them [80]. Reproduced with permission from *Materials Science and Engineering: A*, published by Elsevier, 2005.

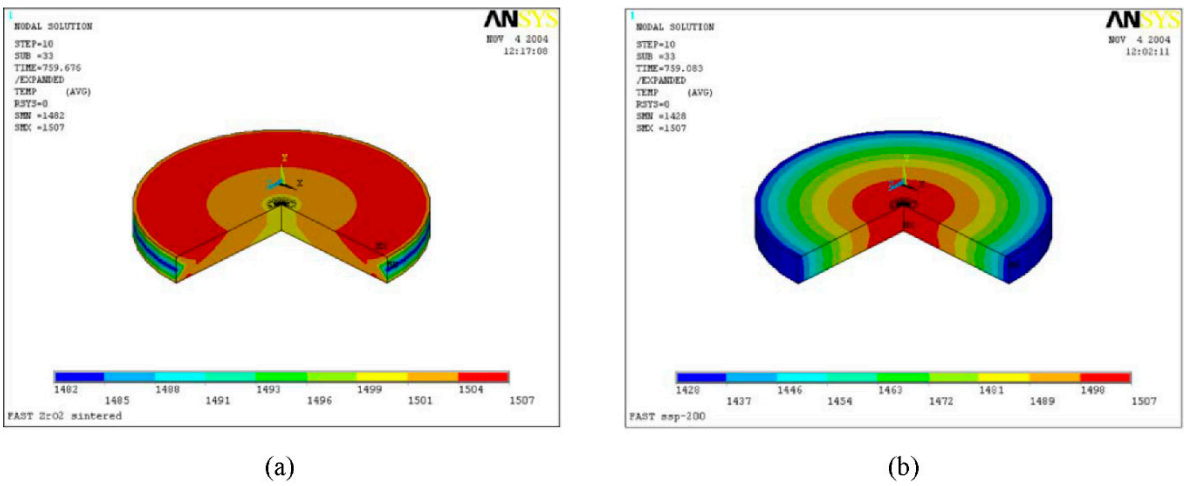

Figure 12. Temperature distribution in insulating ZrO_2 (**a**) and conducting TiN (**b**) samples during holding at 1500 °C [67]. Reproduced with permission from *Acta Materialia*, published by Elsevier, 2005.

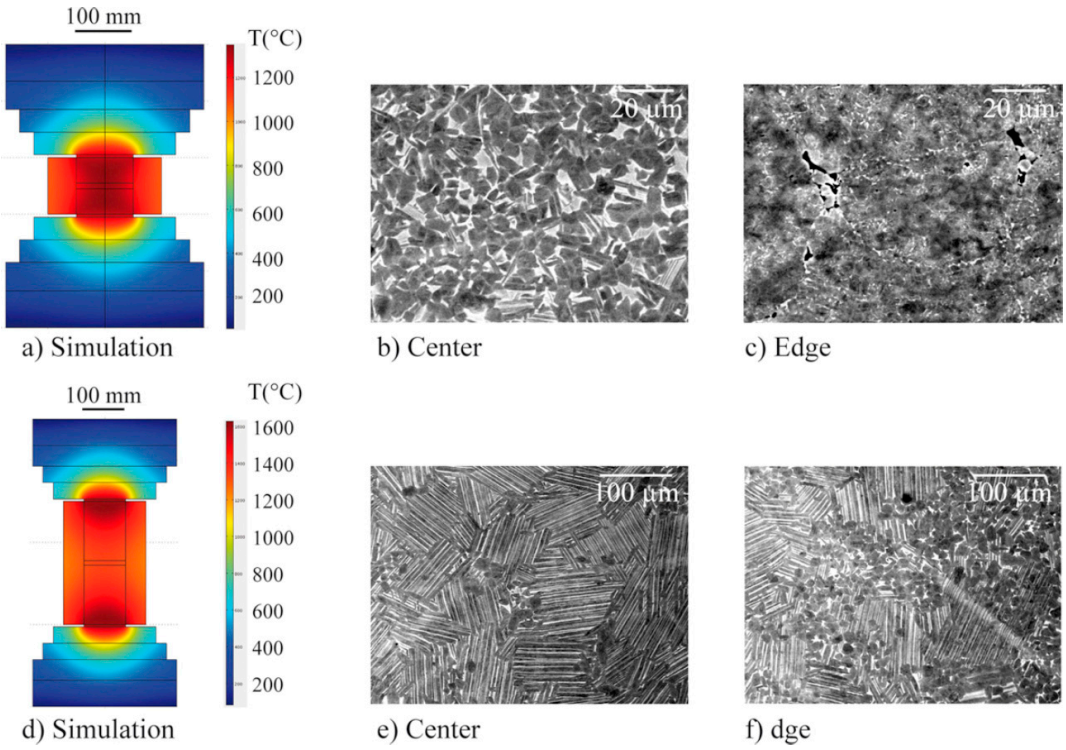

Figure 13. FEM simulations of two SPS setups, compared with metallographic observations of the center and edge of TiAl samples. For setup (**a**), the microstructure of the center is duplex (**b**), and that of the edge is near-γ with some remaining porosities (**c**). This indicates a temperature gradient between the center and the edge of the sample of about 100 °C, in reasonable agreement with the FEM modeling (**a**), which predict a gradient of 125 °C. For setup (**d**), the FEM simulation predicts a temperature gradient between center and edge of the samples of 30 °C. The corresponding microstructures are near lamellar at the center (**e**) and duplex at the edge (**f**), indicating a thermal gradient of 25–50 °C, close to the simulations [74]. Reproduced with permission from *Journal of Materials Processing Technology*, published by Elsevier, 2013.

In summary, the temperature distribution throughout samples during SPS can be accurately predicted with FEM. Indeed, it is a necessary tool for designing molds that minimize thermal gradients and increase the microstructure homogeneity while limiting more expensive and time-consuming experimental testing.

5.1.2. Modeling of Densification Kinetics

There are two ways to model the densification of porous materials: a micromechanical approach based on analytical calculations [81,82] or continuum mechanics derivations [83,84]. The interest of the micromechanical approach is its simplicity, but its limitation is that the model is highly idealized (random dense packing of equal spheres [81]), and can therefore describe too roughly the actual geometrical features of the problem (e.g., powder particles sizes distributed over granulometry ranges). Moreover, the expressions are discontinuous for a density D of 0.9. Despite these shortcomings, it proved to be reasonably accurate. However, to increase results precision, more complex models based on continuum mechanics have been developed notably by Abouaf and Olevsky.

One common input to these calculations is the material constitutive law. For metals, the constitutive laws are most of the time of the following form (Norton relation):

$$\dot{\varepsilon} = A_0 exp\left[-\frac{Q}{RT}\right]\sigma^n, \tag{4}$$

where $\dot{\varepsilon}$: deformation rate, σ: stress, Q: activation energy, n: stress exponent, A_0: material constant, R: gas constant and T: temperature. Using micromechanical or continuum mechanics models, simulations of the densification kinetics have been successfully performed for TiAl [28,73,85], ZrC [86], Ni [77], Fe and Al [87], and Ti-6Al-4V [88]. An example of such

calculations applied to TiAl is shown in Figure 14, in the case of a continuum mechanics model. It can be seen that the calculated densification kinetics reproduces the experimental one with an accuracy better that 5%. Therefore, the models seem to be reasonably accurate.

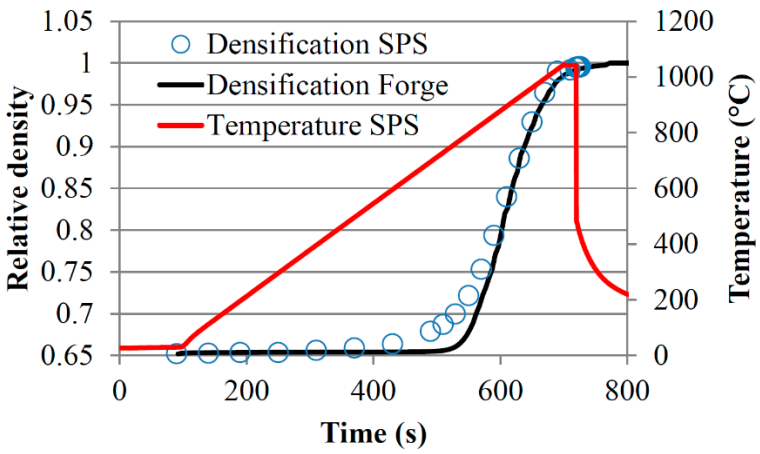

Figure 14. Densification kinetics by SPS of a TiAl alloy, compared with modeling by Forge software and continuum mechanics, using constitutive relations of bulk TiAl [85]. Reproduced with permission from *Intermetallics*, published by Elsevier, 2017.

However, these calculations are very sensitive to the material stress exponent [28]. For example, Figure 15a shows constitutive relations for a recrystallized TiAl powder, in which the activation parameters have been experimentally determined: n = 1.9, and Q = 308 kJ/mol [28]. This law agrees with literature data for bulk TiAl and well captures the SPS kinetics (Figure 15b). However, if n is changed to 3 for a same Q (= 308 kJ/mol) for example, the constitutive relations obtained are still in reasonable agreement with the literature data (Figure 15a), but the model predication is no longer in phase with the experiment (Figure 15b). Therefore, it appears that the models used to predict the SPS densification behavior are very sensitive to the material parameters, which are difficult to accurately determine. Moreover, as can be seen in Figure 15a, the constitutive relations from literature are significantly scattered, and making proper choices of n and Q can be difficult. Therefore, the determination of the material constants has to be carefully carried out.

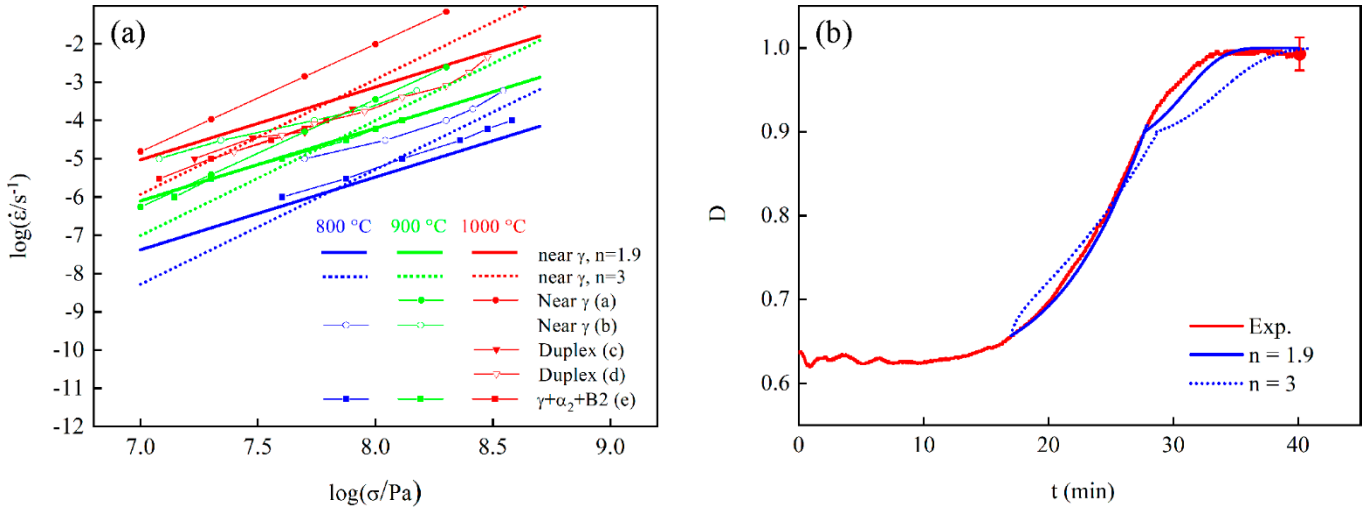

Figure 15. (**a**) Norton laws of a near γ TiAl alloy, taking n = 1.9 and n = 3, the activation energy being identical (Q = 308 kJ/mol). Comparison with literature data of alloys of similar near-γ and duplex microstructures ((a): [85], (b): [89], (c): [90], (d): [91], (e): [92]). (**b**) Densification curves of TiAl (D: relative density, t: time) calculated using n = 1.9 [28], and n = 3, compared with experiment.

5.2. Up-Scaling

Manufacturing big parts is an important issue, to obtain pieces of dimensions suitable for industrial applications. Sintering of metallic disks up to 350 mm in diameter has been reported [93], but a limited number of studies have been published to date. Early works report on processing of large specimens constituted of the following materials: Al [94], Ti (Figure 16) [95], TiAl [74,96]. One of the main difficulties, when processing parts of large dimensions is the presence of thermal and hence microstructure gradients in the materials, which are amplified with respect to those existing in small size samples. Therefore, the geometry of the molds needs to be optimized to homogenize the temperature distribution as previously discussed in Section 5.1.1 by using predictive FEM simulations. Another method is emerging with hybrid SPS machines. Since the temperature gradients are caused by a difference in current density between the center and the edges of the samples, a complimentary external furnace is added to heat the entire mold, thus limiting the temperature gradients. Unfortunately, it seems that no work on this promising approach has been published to date.

Figure 16. Ti composite part of large dimensions (20 cm in diameter), elaborated by SPS [95]. Reproduced with permission from *Materials Science and Engineering: A*, published by Elsevier, 2016.

5.3. Complex Shaping

Finally, shaping of parts of complex geometries is also an important issue, because this would allow to avoid or to limit machining, which can be difficult or even impossible, depending on the material. An early study reported the sintering of WC/Co/Ni screws for extrusion machines by SPS [93]. Unfortunately, little information is provided concerning the methodology. Later on, a method based on the deformation of an interface between a metallic powder and using sacrificial powders transmitting the pressure to the component has allowed forming 3 cm long CoNiCrAlY turbine blades (Figure 17) [97]. Finally, studies have reported on the development of parts in TiAl and NbSi reproducing the shape of turbine blades of aircraft engines, constituted of elongated and massive portions, as long as 10 cm (Figure 18) [30,32,98]. Here, the main challenge lied in compacting regions of different thicknesses such as encountered in this case between the elongated and massive portions. This was overcome by using separate plungers [98].

5.4. Conclusions

The development of simulations of thermoelectric coupling and of densification kinetics proved to be key to optimizing the processing of complex parts. This enabled up-scaling laboratory proof-of-concept to full-size components. Near-net shaping complex, full-scale parts has been successfully demonstrated, opening the doors to a wide range of possibilities, notably for materials hard to obtain with conventional manufacturing techniques.

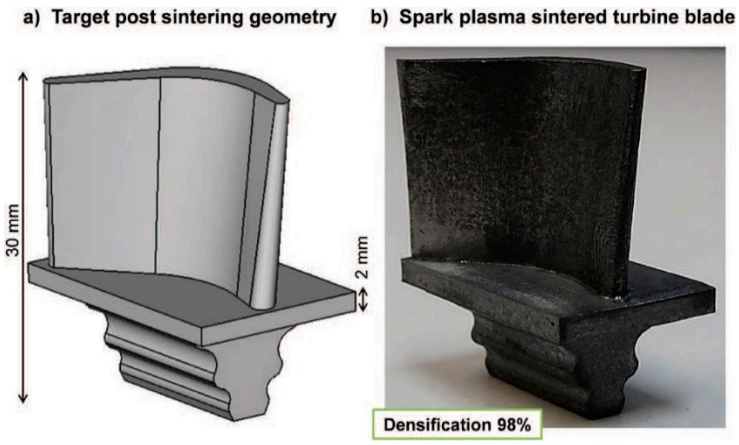

Figure 17. Example of turbine blade in CoNiCrAlY obtained by the deformed interfaces method. (**a**) Target shape. (**b**) Complex part obtained by SPS [97]. Reproduced with permission from *Powder Technology*, published by Elsevier, 2017.

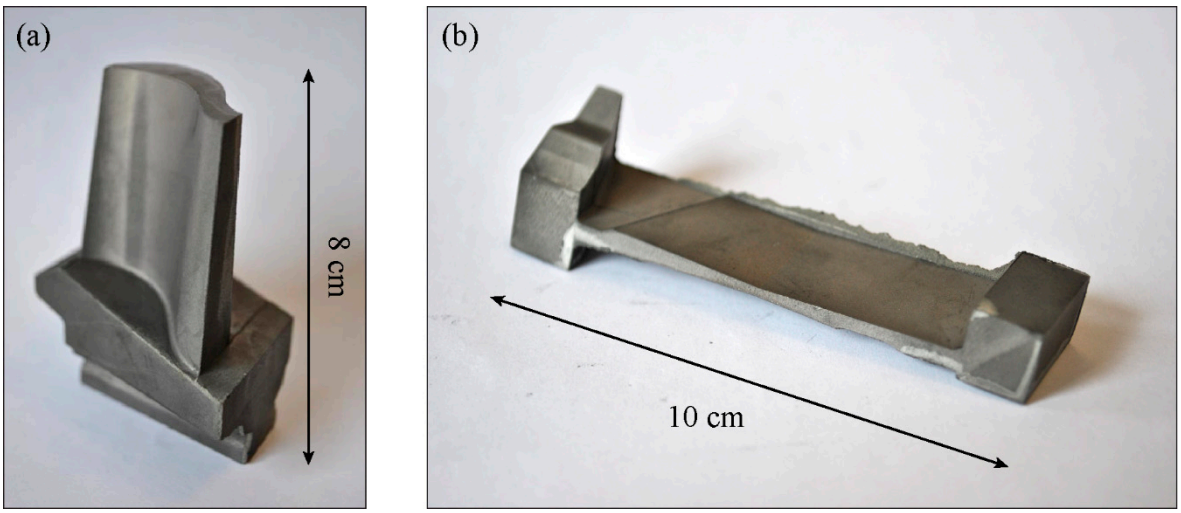

Figure 18. Turbine blade preforms in TiAl (**a**) 8 cm in height [32], and (**b**) 10 cm long [98], shaped by SPS. Reproduced with permission from *Advanced Engineering Materials*, published by John Wiley and Sons, 2015, and from *Springer eBook*, published by Springer Nature, 2019.

However, the challenge is now to implement these approaches in industrial processes, and to develop integrated production sectors. For this purpose, two critical steps can be identified: production of high quality powders, and automation of the SPS process. If satisfactory answers are given to these questions, the SPS technology could potentially experience a large development, because of the elevated properties reached in many cases by the elaborated materials. Therefore, the development of SPS-based processes deserves now increased industrial efforts.

6. General Conclusions

Over the past two decades, SPS has emerged as a technique of choice for producing innovative materials with optimized microstructures and properties, and for shaping complex parts. Despite the absence of demonstrated current-induced effects, the rapid heating by Joule effect allowing short densification cycles appears very efficient at retaining fine, homogeneous microstructures. Design of equilibrium or metastable microstructures can be controlled, depending on the alloy and on the processing conditions. As a result, a wide range of materials can be obtained with improved mechanical properties such as

nanostructured materials, intermetallics, metallic glasses, and high entropy alloys. Moving forward, introducing SPS to new industrial chains will require stepping toward more automated processes, allowing production of parts in larger quantities.

Author Contributions: Methodology, J.-P.M., Z.T., T.V.; software, L.D., T.V.; investigation, J.-P.M., Z.T., T.V.; writing—original draft preparation, J.-P.M.; writing—review and editing, J.-P.M., A.C., L.D., T.V., Z.T., M.T.; supervision, A.C., M.T.; project administration, A.C.; funding acquisition, A.C. All authors have read and agreed to the published version of the manuscript.

Funding: This research was funded by Agence Nationale de la Recherche, grant numbers MF2-ANR-2011-PBS09-020 and IRIS-ANR-08-MAPR-0018. T. Voisin was supported by the Laboratory Directed Research and Development (LDRD) program (21-LW-027) at Lawrence Livermore National Laboratory. T. Voisin's work was performed under the auspices of the U.S. Department of Energy by Lawrence Livermore National Laboratory under contract no. DE-AC52-07NA27344.

Institutional Review Board Statement: Not applicable.

Informed Consent Statement: Not applicable.

Data Availability Statement: Data is contained within the article.

Acknowledgments: SPS experiments were performed using the Sumitomo 2080 SPS machine of the Plateforme Nationale de Frittage Flash du CNRS, Paul Sabatier University, Toulouse, France.

Conflicts of Interest: The authors declare no conflict of interest. The funders had no role in the design of the study; in the collection, analyses, or interpretation of data; in the writing of the manuscript, or in the decision to publish the results.

References

1. Orru, R.; Licheri, R.; Locci, A.M.; Cincotti, A.; Cao, G. Consolidation/synthesis of materials by electric current activated/assisted sintering. *Mater. Sci. Eng. R Rep.* **2009**, *63*, 127–287. [CrossRef]
2. Munir, Z.A.; Anselmi-Tamburini, U.; Ohyanagi, M. The effect of electric field and pres-sure on the synthesis and consolidation of materials: A review of the spark plasma sintering method. *J. Mater. Sci.* **2006**, *41*, 763–777. [CrossRef]
3. Tokita, M. Development of large-size ceramic/metal bulk FGM fabricated by spark plasma sintering. *Mater. Sci. Forum* **1999**, *308–311*, 83–88. [CrossRef]
4. Omori, M. Sintering, consolidation, reaction and crystal growth by the spark plasma system (SPS). *Mater. Sci. Eng. A* **2000**, *287*, 183–188. [CrossRef]
5. Okazaki, K. Electro-discharge consolidation applied to nanocrystalline and RSP/MA powders. *Mater. Sci. Eng. A* **2000**, *287*, 189–197. [CrossRef]
6. Groza, J.R.; Zavaliangos, A. Sintering activation by external electrical field. *Mater. Sci. Eng. A* **2000**, *287*, 171–177. [CrossRef]
7. Ye, J.; Ajdelsztajn, L.; Schoenung, J.M. Bulk nanocrystalline aluminum 5083 alloy fabricated by a novel technique: Cryomilling and spark plasma sintering. *Metall. Mater. Trans. A* **2006**, *37*, 2569–2579. [CrossRef]
8. Yanagisawa, O.; Kuramoto, H.; Matsugi, K.; Komatsu, M. Observation of particle behavior in copper powder compact during pulsed electric discharge. *Mat. Sci. Eng. A* **2003**, *350*, 184–189. [CrossRef]
9. Saunders, T.; Grasso, S.; Reece, M.J. Plasma formation during electric discharge (50 V) through conductive powder compacts. *J. Eur. Ceram. Soc.* **2015**, *35*, 871–877. [CrossRef]
10. Hulbert, D.M.; Anders, A.; Andersson, J.; Lavernia, E.J.; Mukherjee, A.K. A discussion on the absence of plasma in spark plasma sintering. *Scripta Mater.* **2009**, *60*, 835–838. [CrossRef]
11. Song, X.; Liu, X.; Zhang, J. Neck Formation and Self-Adjusting Mechanism of Neck Growth of Conducting Powders in Spark Plasma Sintering. *J. Am. Ceram. Soc.* **2006**, *89*, 494–500. [CrossRef]
12. Xiong, Y.; Liu, D.; Li, Y.; Zheng, B.; Haines, C.; Paras, J.; Martin, D.; Kapoor, D.; Lavernia, E.J.; Schoenung, J.M. Spark plasma sintering of cryomilled nanocrystalline Al alloy—Part I: Microstructure evolution. *Metall. Mater. Trans. A* **2012**, *43*, 327–339. [CrossRef]
13. Diouf, J.S.; Fedrizzi, A.; Molinari, A. A fractographic and microstructural analysis of the neck regions of coarse copper particles consolidated by SPS. *Powder Tech.* **2013**, *221*, 220–227. [CrossRef]
14. Trapp, J.; Kieback, B. Temperature distribution in metallic powder particles during initial stage of field-activated sintering. *J. Am. Ceram. Soc.* **2015**, *98*, 3547–3552. [CrossRef]
15. Collard, C.; Trzaska, Z.; Durand, L.; Chaix, J.M.; Monchoux, J.P. Theoretical and experimental investigations of local overheating at particle contacts in spark plasma sintering. *Powder Tech.* **2017**, *321*, 458–470. [CrossRef]
16. Trzaska, Z.; Collard, C.; Durand, L.; Couret, A.; Chaix, J.M.; Fantozzi, G.; Monchoux, J.P. SPS microscopic mechanisms of metallic systems: Experiments and simulations. *J. Am. Ceram. Soc.* **2019**, *102*, 654–661.

17. Frei, J.M.; Anselmi-Tamburini, U.; Munir, Z.A. Current effects on neck growth in the sintering of copper spheres to copper plates by the pulsed electric current method. *J. Appl. Phys.* **2007**, *101*, 114914. [CrossRef]
18. Ji, G.; Grosdidier, T.; Bozzolo, N.; Launois, S. The mechanisms of microstructure formation in a nanostructured oxide dispersion strengthened FeAl alloy obtained by spark plasma sintering. *Intermetallics* **2007**, *15*, 108–118. [CrossRef]
19. Nowak, S.; Perrière, L.; Dembinski, L.; Tusseau-Nenez, S.; Champion, Y. Approach of the spark plasma sintering mechanism in Zr57Cu20Al10Ni8Ti5 metallic glass. *J. Alloy. Compd.* **2011**, *509*, 1011–1019. [CrossRef]
20. Sprecher, A.F.; Mannan, S.L.; Conrad, H. On the mechanisms for the electroplastic effect in metals. *Acta Metall.* **1986**, *34*, 1145–1162. [CrossRef]
21. Conrad, H.; Sprecher, A.F.; Cao, W.D.; Lu, X.P. Electroplasticity—The effect of electricity on the mechanical properties of metals. *JOM* **1990**, *42*, 28–33. [CrossRef]
22. Guan, L.; Tang, G.; Chu, P.K. Recent advances and challenges in electroplastic manufacturing processing of metals. *J. Mater. Res.* **2010**, *25*, 1215–1224. [CrossRef]
23. Trzaska, Z.; Couret, A.; Monchoux, J.P. Spark plasma sintering mechanisms at the necks between TiAl powder particles. *Acta Mater.* **2016**, *118*, 100–108. [CrossRef]
24. Trzaska, Z.; Cours, R.; Monchoux, J.P. Densification of Ni and TiAl by SPS: Kinetics and microscopic mechanisms. *Metall. Mater. Trans. A* **2018**, *49*, 4849–4859. [CrossRef]
25. Minier, L.; Le Gallet, S.; Grin, Y.; Bernard, F. Influence of the current flow on the SPS sintering of a Ni powder. *J. Alloys. Compd.* **2010**, *508*, 412–418. [CrossRef]
26. Aleksandrova, E.V.; Ilyina, A.M.; Grigoryev, E.G.; Olevsky, E.A. Contribution of electric current into densification kinetics during spark plasma sintering of conductive powder. *J. Am. Ceram. Soc.* **2015**, *98*, 3509–3517. [CrossRef]
27. Collet, R.; Le Gallet, S.; Naimi, F.; Charlot, F.; Bonnefont, G.; Fantozzi, G.; Chaix, J.M.; Bernard, F. Effect of current on the sintering of pre-oxidized copper powders by SPS. *J. Alloy. Compd.* **2017**, *692*, 478–484.
28. Trzaska, Z.; Bonnefont, G.; Fantozzi, G.; Monchoux, J.P. Comparison of densification kinetics of a TiAl powder by spark plasma sintering and hot pressing. *Acta Mater.* **2017**, *135*, 1–13. [CrossRef]
29. Bewlay, B.P.; Nag, S.; Suzuki, A.; Weimer, M.J. TiAl alloys in commercial aircraft engines. *Mater. High Temp.* **2016**, *33*, 549–559. [CrossRef]
30. Couret, A.; Voisin, T.; Thomas, M.; Monchoux, J.P. Development of a TiAl alloy by spark plasma sintering. *JOM* **2017**, *69*, 2576–2582. [CrossRef]
31. Voisin, T.; Monchoux, J.P.; Perrut, M.; Couret, A. Obtaining of a fine near-lamellar microstructure in TiAl alloys by Spark Plasma Sintering. *Intermetallics* **2016**, *71*, 88–97. [CrossRef]
32. Voisin, T.; Monchoux, J.P.; Durand, L.; Karnatak, N.; Thomas, M.; Couret, A. An innovative way to produce-TiAl blades: Spark plasma sintering. *Adv. Eng. Mater.* **2015**, *17*, 1408–1413. [CrossRef]
33. Voisin, T.; Monchoux, J.P.; Thomas, M.; Deshayes, C.; Couret, A. Mechanical properties of the TiAl IRIS alloy. *Metall. Mater. Trans. A* **2016**, *47*, 6097–6108. [CrossRef]
34. Zhang, Z.; Wang, F.; Lee, S.; Liu, Y.; Cheng, J.; Liang, Y. Microstructure characteristic, mechanical properties and sintering mechanism of nanocrystalline copper obtained by SPS process. *Mat. Sci. Eng. A* **2009**, *523*, 134–138. [CrossRef]
35. Shearwood, C.; Fu, Y.; Yu, L.; Khor, K. Spark plasma sintering of TiNi nano-powder. *Scripta Mater.* **2005**, *52*, 455–460. [CrossRef]
36. Kellogg, F.; McWilliams, B.; Sietins, J.; Giri, A.; Cho, K. Comparison of SPS processing behavior between as atomized and cryomilled aluminum alloy 5083 powder. *Metall. Mater. Trans A* **2017**, *48*, 5492–5499. [CrossRef]
37. El-Atwania, O.; Quach, D.V.; Efe, M.; Cantwell, P.R.; Heim, B.; Schultz, B.; Stach, E.A.; Groza, J.R.; Allain, J.P. Multimodal grain size distribution and high hardness in fine grained tungsten fabricated by spark plasma sintering. *Mat. Sci. Eng. A* **2011**, *528*, 5670–5677. [CrossRef]
38. Dirras, G.; Bouvier, S.; Gubicza, J.; Hasni, B.; Szilagyi, T. Mechanical characteristics under monotonic and cyclic simple shear of spark plasma sintered ultrafine-grained nickel. *Mat. Sci. Eng. A* **2009**, *526*, 201–210. [CrossRef]
39. Bui, Q.H.; Dirras, G.; Ramtani, S.; Gubicza, J. On the strengthening behavior of ultrafine-grained nickel processed from nanopowders. *Mat. Sci. Eng. A* **2010**, *527*, 3227–3235. [CrossRef]
40. Dutel, G.D.; Tingaud, D.; Langlois, P.; Dirras, G. Nickel with multimodal grain size distribution achieved by SPS: Microstructure and mechanical properties. *J. Mater. Sci.* **2012**, *47*, 7926–7931. [CrossRef]
41. Farbaniec, L.; Dirras, G.; Krawczynska, A.; Mompiou, F.; Couque, H.; Naimi, F.; Bernard, F.; Tingaud, D. Powder metallurgy processing and deformation characteristics of bulk multimodal nickel. *Mater. Charac.* **2014**, *94*, 126–137. [CrossRef]
42. Tingaud, D.; Jenei, P.; Krawczynska, A.; Mompiou, F.; Gubicza, J.; Dirras, G. Investigation of deformation micro-mechanisms in nickel consolidated from a bimodal powder by spark plasma sintering. *Mater. Charac.* **2015**, *99*, 118–127. [CrossRef]
43. Naimi, F.; Minier, L.; Le Gallet, S.; Couque, H.; Bernard, F. Dense nanostructured nickel produced by SPS from mechanically activated powders: Enhancement of mechanical properties. *J. Nanomater.* **2013**, *2013*, 674843. [CrossRef]
44. García de la Cruz, L.; Flipon, B.; Keller, C.; Martinez, M.; Hug, E. Nanostructuration of metals via spark plasma sintering using activated powder obtained by ball-milling: Impact on the strain-hardening mechanisms. *AIP Conf. Proc.* **2017**, *1896*, 200002.
45. García de la Cruz, L.; Martinez, M.; Keller, C.; Hug, E. Achieving good tensile properties in ultrafine grained nickel by spark plasma sintering. *Mat. Sci. Eng. A* **2020**, *772*, 138770. [CrossRef]

46. Vajpai, S.K.; Yu, H.; Ota, M.; Watanabe, I.; Dirras, G.; Ameyama, K. Three-dimensionally gradient and periodic harmonic structure for high performance advanced structural materials. *Mater. Trans.* **2016**, *57*, 1424–1432. [CrossRef]
47. Dirras, G.; Tingaud, D.; Ueda, D.; Hocini, A.; Ameyama, K. Dynamic Hall-Petch versus grain-size gradient effects on the mechanical behavior under simple shear loading of β-titanium Ti-25Nb-25Zr alloys. *Mater. Lett.* **2017**, *206*, 214–216. [CrossRef]
48. Dirras, G.; Ueda, D.; Hocini, A.; Tingaud, D.; Ameyama, K. Cyclic shear behavior of conventional and harmonic structure-designed Ti-25Nb-25Zr β-titanium alloy: Back-stress hardening and twinning inhibition. *Scripta Mater.* **2017**, *138*, 44–47. [CrossRef]
49. Ueda, D.; Dirras, G.; Hocini, A.; Tingaud, D.; Ameyama, K.; Langlois, P.; Vrel, D.; Trzaska, Z. Data on processing of Ti-25Nb-25Zr β-titanium alloys via powder metallurgy route: Methodology, microstructure and mechanical properties. *Data Brief* **2018**, *17*, 703–708. [CrossRef]
50. Charpentier, M. Hétérogénéités Héritées de la Solidification et Formation des Microstructures Dans L'alliage Ti48Al2Cr2Nb. Contribution au Développement des Alliages Intermétalliques de Base γ-TiAl. Ph.D. Thesis, Ecole des Mines, Nancy, France, 2003.
51. Miller, S.A.; Murphy, R.J. A gas-water atomization process for producing amorphous powders. *Scripta Metall.* **1979**, *13*, 673–676. [CrossRef]
52. Perrière, L.; Champion, Y.; Bernard, F. Spark plasma sintering of metallic glasses. In *Spark Plasma Sintering of Materials*; Cavaliere, P., Ed.; Springer: Cham, Switzerland, 2019; pp. 291–335.
53. Perrière, L.; Thai, M.T.; Tusseau-Nenez, S.; Blétry, M.; Champion, Y. Spark plasma sintering of a Zr-based metallic glass. *Adv. Eng. Mater.* **2011**, *13*, 581–586. [CrossRef]
54. Liu, Y.; Wang, J.S.; Fang, Q.H.; Liu, B.; Wu, Y.; Chen, S.Q. Preparation of superfine-grained high entropy alloy by spark plasma sintering gas atomized powder. *Intermetallics* **2016**, *68*, 16–22. [CrossRef]
55. Zhou, P.F.; Xiao, D.H.; Wu, Z.; Song, M. Microstructure and mechanical properties of AlCoCrFeNi high entropy alloys produced by spark plasma sintering. *Mater. Res. Express* **2019**, *6*, 0865e7. [CrossRef]
56. Fu, Z.; Chen, W.; Wen, H.; Zhang, D.; Chen, Z.; Zheng, B.; Zhou, Y.; Lavernia, E.J. Microstructure and strengthening mechanism in an fcc structured single-phase nanocrystalline Co25Ni25Fe25Al7.5Cu17.5 high-entropy alloy. *Acta Mater.* **2016**, *107*, 59–71. [CrossRef]
57. Moravcik, I.; Cizek, J.; Zapletal, J.; Kovacova, Z.; Vesely, J.; Minarik, P.; Kitzmantel, M.; Neubauer, E.; Dlouhy, I. Microstructure and mechanical properties of Ni1,5Co1,5CrFeTi0,5 high entropy alloy fabricated by mechanical alloying and spark plasma sintering. *Mater. Des.* **2017**, *119*, 141–150. [CrossRef]
58. Praveen, S.; Murty, B.S.; Kottada, R.S. Alloying behavior in multi-component AlCoCrCuFe and NiCoCrCuFe high entropy alloys. *Mater. Sci. Eng. A* **2012**, *534*, 83–89. [CrossRef]
59. Chen, Z.; Chen, W.; Wu, B.; Cao, X.; Liu, L.; Fu, Z. Effects of Co and Ti on microstructure and mechanical behaviour of Al0.75FeNiCrCo high entropy alloy prepared by mechanical alloying and spark plasma sintering. *Mater. Sci. Eng. A* **2015**, *648*, 217–224. [CrossRef]
60. Wang, P.; Cai, H.; Cheng, X. Effect of Ni/Cr ratio on phase, microstructure and mechanical properties of $Ni_xCoCuFeCr_{2-x}$ (x = 1.0, 1.2, 1.5, 1.8 moL) high entropy alloys. *J. Alloy. Compd.* **2016**, *662*, 20–31. [CrossRef]
61. Zhang, A.; Han, J.; Su, B.; Meng, J. A novel CoCrFeNi high entropy alloy matrix selflubricating composite. *J. Alloy. Compd.* **2017**, *725*, 700–710. [CrossRef]
62. Suryanarayana, C. Mechanical alloying and milling. *Prog. Mater. Sci.* **2001**, *46*, 1–184. [CrossRef]
63. Jabbar, H.; Couret, A.; Durand, L.; Monchoux, J.P. Identification of microstructural mechanisms during densification of a TiAl alloy by spark plasma sintering. *J. Alloy. Compd.* **2011**, *509*, 9826–9835. [CrossRef]
64. Yucheng, W.; Zhengyi, F. Study of temperature field in spark plasma sintering. *Mater. Sci. Eng. B* **2002**, *90*, 34–37. [CrossRef]
65. Matsugi, K.; Kuramoto, H.; Hatayama, T.; Yanagisawa, O. Temperature distribution at steady state under constant current discharge in spark sintering process of Ti and Al2O3 powders. *J. Mater. Process. Tech.* **2004**, *146*, 274–281. [CrossRef]
66. Zavaliangos, A.; Zhang, J.; Krammer, M.; Groza, J.R. Temperature evolution during field activated sintering. *Mater. Sci. Eng. A* **2004**, *379*, 218–228. [CrossRef]
67. Vanmeensel, K.; Laptev, A.; Hennicke, J.; Vleugels, J.; Van der Biest, O. Modelling of the temperature distribution during field assisted sintering. *Acta Mater.* **2005**, *53*, 4379–4388. [CrossRef]
68. Wang, X.; Casolco, S.R.; Xu, G.; Garay, J.E. Finite element modeling of electric current activated sintering: The effect of coupled electrical potential, temperature and stress. *Acta Mater.* **2007**, *55*, 3611–3622. [CrossRef]
69. McWilliams, B.; Zavaliangos, A. Multi-phenomena simulation of electric field assisted sintering. *J. Mater. Sci.* **2008**, *43*, 5031–5035. [CrossRef]
70. Molénat, G.; Durand, L.; Galy, J.; Couret, A. Temperature control in spark plasma sintering: An FEM approach. *J. Metallurgy* **2010**, 145431. [CrossRef]
71. Muñoz, S.; Anselmi-Tamburini, U. Temperature and stress fields evolution during spark plasma sintering processes. *J. Mater. Sci.* **2010**, *45*, 6528–6539. [CrossRef]
72. Song, Y.; Li, Y.; Zhou, Z.; Lai, Y.; Ye, Y. A multi-field, coupled FEM model for one-step forming process of spark plasma sintering considering local densification of powder material. *J. Mater. Sci.* **2011**, *46*, 5645–5656. [CrossRef]
73. Mondalek, P.; Silva, L.; Bellet, M. A numerical model for powder densification by SPS technique. *Adv. Eng. Mater.* **2011**, *13*, 587–593. [CrossRef]

74. Voisin, T.; Durand, L.; Karnatak, N.; Le Gallet, S.; Thomas, M.; Le Berre, Y.; Castagné, J.F.; Couret, A. Temperature control during Spark Plasma Sintering and application to up-scaling and complex shaping. *J. Mater. Proc. Tech.* **2013**, *213*, 269–278. [CrossRef]
75. Wolff, C.; Mercier, S.; Couque, H.; Molinari, A. Modeling of conventional hot compaction and spark plasma sintering based on modified micromechanical models of porous materials. *Mech. Mater.* **2012**, *49*, 72–91. [CrossRef]
76. Pavia, A.; Durand, L.; Ajustron, F.; Bley, V.; Chevallier, G.; Peigney, A.; Estournès, C. Electro-thermal measurements and finite element method simulations of a spark plasma sintering device. *J. Mater. Process. Tech.* **2013**, *213*, 1327–1336. [CrossRef]
77. Wolff, C.; Mercier, S.; Couque, H.; Molinari, A.; Bernard, F.; Naimi, F. Thermal-electrical-mechanical simulation of the nickel densification by Spark Plasma Sintering. Comparison with experiments. *Mech. Mater.* **2016**, *100*, 126–147. [CrossRef]
78. Achenani, Y.; Saâdaoui, M.; Cheddadi, A.; Bonnefont, G.; Fantozzi, G. Finite element modeling of spark plasma sintering: Application to the reduction of temperature inhomogeneities, case of alumina. *Mater. Des.* **2017**, *116*, 504–514. [CrossRef]
79. Manière, C.; Pavia, A.; Durand, L.; Chevallier, G.; Afanga, K.; Estournès, C. Finite-element modeling of the electro-thermal contacts in the spark plasma sintering process. *J. Eur. Ceram. Soc.* **2016**, *36*, 741–748. [CrossRef]
80. Anselmi-Tamburini, U.; Gennari, S.; Garay, J.E.; Munir, Z.A. Fundamental investigations on the spark plasma sintering/synthesis process: II. Modeling of current and temperature distributions. *Mater. Sci. Eng. A* **2005**, *394*, 139–148. [CrossRef]
81. Arzt, E.; Ashby, M.F.; Easterling, K.E. Practical applications of hot-isostatic pressing dia-grams: Four case studies. *Metall. Trans. A* **1983**, *14*, 211–221. [CrossRef]
82. Helle, A.S.; Easterling, K.E.; Ashby, M.F. Hot-isostatic pressing diagrams: New develop-ments. *Acta Metall.* **1985**, *33*, 2163–2174. [CrossRef]
83. Abouaf, M. Modélisation de la Compaction de Poudres Métalliques Frittées—Approche par la Mécanique des Milieux Continus. Ph.D. Thesis, Institut National Polytechnique, Grenoble, France, 1985.
84. Olevsky, E.A. Theory of sintering: From discrete to continuum. *Mat. Sci. Eng. R* **1998**, *23*, 41–100. [CrossRef]
85. Martins, D.; Grumbach, F.; Manière, C.; Sallot, P.; Mocellin, K.; Bellet, M.; Estournès, C. In-situ creep law determination for modeling spark plasma sintering of TiAl 48-2-2 powder. *Intermetallics* **2017**, *86*, 147–155. [CrossRef]
86. Wei, X.; Back, C.; Izhvanov, O.; Khasanov, O.L.; Haines, C.D.; Olevsky, E.A. Spark plasma sintering of commercial zirconium carbide powders: Densification behavior and mechanical properties. *Materials* **2015**, *8*, 6043–6061. [CrossRef]
87. Manière, C.; Durand, L.; Chevallier, G.; Estournès, C. A spark plasma sintering densification modeling approach: From polymer, metals to ceramics. *J. Mater. Sci.* **2018**, *53*, 7869–7876. [CrossRef]
88. Manière, C.; Kus, U.; Durand, L.; Mainguy, R.; Huez, J.; Delagnes, D.; Estournès, C. Identification of the Norton-Green compaction model for the prediction of the Ti-6Al-4V densification during the spark plasma sintering process. *Adv. Eng. Mater.* **2016**, *18*, 1720–1727. [CrossRef]
89. Sun, J.; He, Y.H.; Wu, J.S. Characterization of low-temperature superplasticity in a thermomechanically processed TiAl based alloy. *Mat. Sci. Eng. A* **2002**, *329–331*, 885–890. [CrossRef]
90. Sun, J.; Wu, J.S.; He, Y.H. Superplastic properties of a TiAl based alloy with a duplex microstructure. *Mater. Sci.* **2000**, *35*, 4919–4922. [CrossRef]
91. Cheng, S.C.; Wolfenstine, J.; Sherby, O.D. Superplastic behavior of 2-phase titanium aluminides. *Metall. Trans. A* **1992**, *23*, 1509–1513. [CrossRef]
92. Nieh, T.G.; Hsiung, L.M.; Wadsworth, J. Superplastic behavior of a powder metallurgy TiAl alloy with a metastable microstructure. *Intermetallics* **1999**, *7*, 163–170. [CrossRef]
93. Tokita, M. The potential of spark plasma sintering (SPS) method for the fabrication on an industrial scale of functionally graded materials. *Adv. Sci. Tech.* **2010**, *63*, 322–331. [CrossRef]
94. Sweet, G.A.; Brochu, M.; Hexemer, R.L.; Donaldson, I.W.; Bishop, D.P. Microstructure and mechanical properties of air atomized aluminum powder consolidated via spark plasma sintering. *Mater. Sci. Eng. A* **2014**, *608*, 273–282. [CrossRef]
95. Lagos, M.A.; Agote, V.; Atxaga, G.; Adarraga, O.; Pambaguian, L. Fabrication and characterisation of Titanium Matrix Composites obtained using a combination of Self propagating High temperature Synthesis and Spark Plasma Sintering. *Mater. Sci. Eng. A* **2016**, *655*, 44–49. [CrossRef]
96. Naanani, S.; Hantcherli, M.; Hor, A.; Mabru, C.; Monchoux, J.P.; Couret, A. Study of the low cyclic behaviour of the IRIS alloy at high temperature. *MATEC Web Conf.* **2018**, *165*, 06007. [CrossRef]
97. Manière, C.; Nigito, E.; Durand, L.; Weibel, A.; Beynet, Y.; Estournes, C. Spark plasma sintering and complex shapes: The deformed interfaces approach. *Powder Tech.* **2017**, *320*, 340–345. [CrossRef]
98. Voisin, T.; Monchoux, J.P.; Couret, A. Near-net shaping of titanium-aluminum jet engine turbine blades by SPS. In *Spark Plasma Sintering of Materials*; Cavaliere, P., Ed.; Springer: Cham, Switzerland, 2019; pp. 713–737.